Authors Version

Evaluation of Molten Sand, Dust, and Ash Infiltrating Thermal Barrier Coatings: Numerical and Analytical Approaches

B. Cavainolo[1] , R. Naraparaju[2] ,2 M-R. Kabir[2] and M. P. Kinzel[3]

1)Mechanical and Aerospace Engineering, University of Central Florida. 12760 Pegasus Drive Orlando, FL 32816. United States.

2)Institute of Materials Research, German Aerospace Center (DLR). Linder Höhe, 51147 Köln, Germany.

3) Aerospace Engineering, EEmbry-Riddle Aeronautical University. 1 Aerospace Boulevard Daytona Beach, FL 32114. United States

Physics of Fluids 36, 113373 (2024)

doi: 10.1063/5.0234882

Evaluation of Molten Sand, Dust, and Ash Infiltrating Thermal Barrier Coatings: Numerical and Analytical Approaches

B. Cavainolo,[1] R. Naraparaju,[2] M-R. Kabir,[3] and M. P. Kinzel[4]
[1)]*Mechanical and Aerospace Engineering, University of Central Florida. 12760 Pegasus Drive Orlando, FL 32816. United States.*
[2)]*Institute of Materials Research, German Aerospace Center (DLR). Linder Höhe, 51147 Köln, Germany.*
[3)]*Institute of Materials Research, German Aerospace Center (DLR). Linder Höhe, 51147 Köln, Germany*
[4)]*Aerospace Engineering, Embry-Riddle Aeronautical University. 1 Aerospace Boulevard Daytona Beach, FL 32114. United States.*

(*Electronic mail: brendon.cavainolo@ucf.edu)

(Dated: 28 October 2024)

Calcium-Magnesium-Alumino-Silicate (CMAS) is a category of atmospheric debris in the form of dirt, sand, and ash that damage thermal barrier coatings (TBC) in aircraft engines. The damage is not a direct result of erosion, but rather, CMAS melts in engines and impacts the TBCs. In this state, the CMAS can infiltrate the TBC microstructure which leads to surface damage from secondary stresses associated with thermal loading and expansion in the micro-structure. Understanding the fluid dynamic processes of the infiltration is key to develop TBCs that mitigate TBC infiltration damage. The fluidic processes are evaluated using micro-structure-resolving, finite-volume, multi-phase, volume-of-fluid computational fluid dynamics simulations (CFD). CFD results using experimentally measured temperature-dependent polynomial CMAS viscosity are compared to experiments and analytical models and indicate that feathery-shaped microstructure in TBCs inhibit CMAS infiltration more than rectangular channel TBCs. Such observations are conditional on the Ohnesorge Number (Oh). For low Oh values, the rectangular channel reduces infiltration, while the feathery channel is more effective at reducing infiltration for higher Oh values. Three-dimensional CFD results under-predicted experimental and theoretical infiltraiton depth. A novel infiltration model for feathery channels, the "Feathery Pipe-Network Model" (FPNM) was implemented. FPNM results agree with experiments and other analytical models. Using FPNM in conjunction with the concentric-pipe model achieves a 25% margin-of-error when evaluated against experimental results. This is a 15% reduction in error compared to using the open-pipe and concentric-pipe models as the prediction. This enhanced prediction model can lead to safer and more cost-effective aircraft operation in debris-laden environments.

I. INTRODUCTION

Ingestion of Calcium-Magnesium-Alumino-Silicate (CMAS) particles by airplane engines threatens the safety and durability of aircraft. When CMAS particles enter the engine, the high temperatures melt the particles that can later be deposited and solidify on engine components[1]. The deposition of these melted particles can damage the thermal barrier coatings that protect the high-pressure turbine blades and combustor liners, which leads to overheating and damaged surfaces that can cause engine stall[1]. The issue is not limited to engines on fixed-wing aircraft. Helicopters operating in sandy desert environments are at even higher risk of CMAS damage through engines ingesting sand kicked up during take off and landing[2]. It is clear that the relationship of CMAS to aircraft safety and durability is crucial to understand how CMAS behaves inside aircraft engines to prevent damage to both airplanes and the global economy.

Thermal Barrier Coatings (TBCs) are outer ceramic layers applied to aircraft engine components, such as high-pressure turbine blades, to protect them from prolonged exposure to heat[3]. These coatings can reduce component temperatures[4] from around 1700 K to 1200 K. As higher temperature turbines are required for more efficient and higher thrust applications, such coatings are essential for the heat-related aspects of engine design. These TBC systems can utilize a variety of materials and be implemented using different methods. One approach uses electron-beam physical vapor deposition (EB-PVD) to manufacture 7% yttria-stabilized zirconia (7YSZ) coatings. 7YSZ coatings manufactured with this method are favored for their aerodynamic performance and strain compliance benefits over TBCs manufactured with other methods. Note that the top coat is the layer most susceptible to CMAS infiltration[5]. The columnar microstructure of an EB-PVD coating is shown in Fig. 1, which shows both "normal" and "feathery" TBCs. These features indicate potential microstructure patterns in TBC coating design.

Melted CMAS infiltrates the inter-columnar gaps, and due to the established thermal gradient throughout the coating thickness, some areas of the coating are infiltrated, while others are not. As a result of this, an overall decrease in strain tolerance, and an increase in thermal conductivity is observed, as well as a discrepancy in thermal expansion coefficient between the infiltrated and uninfiltrated regions[7–9]. This causes the coating to become susceptible to delamination, if the coating is infiltrated beyond a critical depth[10]. The CMAS attack also causes a sintering phenomena to occur, which also erodes TBCs[11]. As manufacturers seek to help aero-engines achieve higher temperatures for efficiency gains, molten CMAS is becoming more of a problem[12], because the viscosity of CMAS

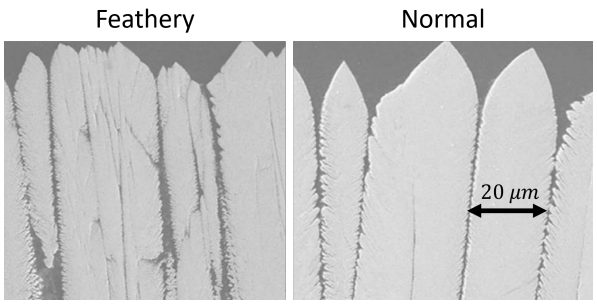

FIG. 1: Feathery and parallel microstructure for EB-PVD TBCs under magnification[6]. These side views were obtained by extracting a cross-section of TBC samples.

is temperature dependent[6]. Thus, higher engine operating temperatures make the CMAS less viscous, and increases its ability to infiltrate the coatings. Depending on composition, most forms of CMAS melt between 1150 - 1250 °C[13–16].The sintering occurs when the molten CMAS comes into contact with the TBC. In one such case, molten volcanic ash interacted with a YSZ TBC to form yttria-iron garnet[17].

Previous simulation-based infiltration models have used a finite-element based approach[4,18], but this approach comes with several challenges, including difficulties associated with surface tension forces. Kabir and Sirigiri's approach uses a coupled Euler-Lagrange methodology. Here, the TBC is a rigid-body in a Lagrangian domain, and the molten CMAS is a fluid in an Eulerian domain. However, the Eulerian domain is not multiphase (i.e. the air-CMAS interface is not explicitly resolved). Void cells are used instead of an air-phase, and surface tension forces are modeled at the free-surface.

This paper proposes the application of finite-volume method (more specifically and as described in Section II, the Volume-of-Fluid Method (VOF)) computational fluid dynamics (CFD), to evaluate CMAS infiltration using first principles methods for several idealized TBC geometries. Overall, the approach has the potential to push the understanding of infiltration processes. Previous work using this methodology has determined that experimental measurements for viscosity led to more accurate infiltration times. However, there was a large discrepancy between simulated and experimental infiltration times[19].

Many theoretical models exist to evaluate problems that are similar to the CMAS/TBC Infiltration Problem. TBC columns are considered capillary columns[6]. Thus, seepage-based theoretical models for soil flows may be applicable. One such theoretical model is Layered-Infiltration Theory in which water infiltration depth in soil is estimated based on the properties in the different layers of soil.[20]. The open-pipe model (OPM) and concentric-pipe model (CPM) have been derived from soil-based flows, and applied to the CMAS/TBC infiltration problem[21–23]. A theoretical model for predicting capillary imbibition in rocks was developed by correcting the Hagen–Poiseuille equation to account for pore shape and orientation[24]. The Lucas-Washburn equation was also modified to model large porous structures instead of isolated columnar channels[25]. There is no shortage of theoretical models that could help solve the CMAS/TBC problem. However, all of these models would need to be expanded and specifically tuned to accommodate CMAS/TBC infiltration. The OPm and CPM sought to accomplish this, but results fell within a wide margin of error compared to experiments[23]. OPM and CPM assume a large porous medium, and the microstructure boils down to a couple of geometric parameters. So, a new thoertical model is needed to accurately capture effects complicated microstructures, such as the "feathery" microstructure in Fig. 1. So, additionally, this work proposes the "Feathery Pipe-network Model" (FPNM) as a way to describe the flow in an isolated feathery TBC columnar gap.

In summary, this work seeks to do the following: 1) Provide details of a methodology in which CMAS infiltration into a TBC is directly resolved using numerical simulation 2) Compare the directly-resolved simulation results to expected results from the analytical pipe models[23] (Shown in Appendix A), the FPNM, and previous experiments measured at the German Aerospace Center (DLR)[23]. 3) Characterize the infiltration process based on physical and geometric properties.

II. METHODS

A. Computational Fluid Dynamics Simulations

The simulation methodology used in our efforts[19,26] is based on the finite-volume-based, VOF CFD approach. These models are built into Star-CCM+[27], and are not unique or novel. Hence, the numerical methods will only be described briefly, and the reader is referred to the Star-CCM+ User Manual for more information on the specifics[27]. However, the implementation of these methods is novel in that VOF has not yet been used to analyze the CMAS infiltration problem. Lattice-Boltzmann methods are commonly used to resolve complicated geometries[28]. However, it has been shown that Navier-Stokes based methods are capable of resolving microfluidic problems as well[29].

The first step in simulating the infiltration of CMAS was to ensure the VOF method is a valid approach for capturing the melting-solidification of a CMAS particle. A mesh independence study was conducted in previous work[26], and it is shown that melting particles between the solidus and liquidus temperatures of CMAS can be accurately resolved with the VOF method. For multiphase physics, the Eulerian Multiphase Volume-of-Fluid method was used to simulate the interactions between the two Eulerian phases, air, and CMAS. Modeling surface tension properly is critical as the infiltration is driven by capillary forces. The governing equations of the VOF-CFD model from Star-CCM+[27] include conservation equations for mass,

$$\frac{\partial}{\partial t}\int_V \rho dV + \oint_A v\cdot d\vec{A} = \int_V (S)\,dV\ ,\ S = \sum_i S_{\alpha_i}\rho_i, \quad (1)$$

momentum,

$$\begin{aligned}&\frac{\partial}{\partial t}\int_V \rho v dV + \oint_A \rho v \times v \cdot\ dA \\ &= \oint_A \rho I \cdot d\,A + \oint_A T \cdot d\,A + \int_V \rho g dV \\ &+ \int_V f_b dV - \sum_i \int_A a_i \rho_i v_{d,i} \times v_{d,i} dA\end{aligned} \tag{2}$$

and energy,

$$\begin{aligned}&\frac{\partial}{\partial t}\int_V \rho E dV + \oint_A \left[\rho H v + p + \alpha_i \rho_i H_i v_{d,i}\right] \cdot dA = \\ &= -\oint_A \dot{q}'' \cdot dA \\ &+ \oint_A T \cdot v dA + \int_V S_E dV + \int_V f_b dV.\end{aligned} \tag{3}$$

Equations 1-3 couple to the Eulerian Multiphase VOF approach, which solves a transport equation for volume fraction of a phase i ($\alpha_i = V_i/V$) and is formulated as follows

$$\begin{aligned}&\frac{\partial}{\partial t}\int_V \alpha_i dV + \oint_A \alpha_i v \cdot dA \\ &= \int_V \left(S_{\alpha_i} - \frac{\alpha_i}{\rho_i}\frac{D\rho_i}{Dt}\right) dV \\ &- \int_V \frac{1}{\rho_i}\nabla \cdot \left(\alpha_i \rho_i v_{d,i}\right) dV\end{aligned} \tag{4}$$

In these equations, the subscript i denotes a particular phase (in this case, air or CMAS), and S_{α_i} is a source term that controls phase change. This equation is discretized using High-Resolution Interface Capturing (HRIC). HRIC blends the upwind and downwind solution around an interface to satisfy a Courant number limit (i.e. Co = 1.0), and if the Courant number is exceeded, then the HRIC scheme reverts back to a standard upwind scheme, which results in a smeared interface. This smeared interface can be corrected by implementing temporal subcycling. The general idea of temporal subcycling is shown in Eq. 5, where the right-hand side of the equation is a single source term that combines the right-hand side contributions from Eq. 4. The use of a multiphase model is a key departure from Kabir and Sirigiri's work[4,18] because it allows for direct resolution of the capillary effects at the air-CMAS interface, as opposed to a modeled free-surface boundary driven downward with a prescribed capillary pressure.

$$\begin{aligned}&\alpha^{n+\Delta t} V - \alpha^n V + \int_{t^n}^{t^{n+\Delta t}} (\sum_A \alpha_f(s) v \cdot da) \\ &= \int_{t^n}^{t^{n+\Delta t}} (S(\alpha(s),...) ds\end{aligned} \tag{5}$$

In this work, an implicit multi-stepping version of this temporal subcycling is employed, which gives an unconditionally stable solution, and a sharp interface is achieved if $\frac{CFL}{N_{imp}} \leqslant 0.5$. The sub-iterations calculated with Eq. 6 are summed to get the overall contribution for the whole time step.

$$\begin{aligned}&\alpha_{i+1} V - \alpha_i V + \tau(\sum_A \alpha_{f,i+1}(\tau) v \cdot da) \\ &= \tau(S(\alpha^{n+\Delta t},...)\ for\ i = 1,2,...,N\end{aligned} \tag{6}$$

A drawback of using the VOF method for the infiltration is the very small time steps required to resolve the CMAS infiltration. So, adaptive time-stepping combined with sub-iterations was used to balance computational speed and accuracy. A free-surface condition was enforced so that the Courant number ($Co = \frac{u\Delta t}{\Delta x}$) at the interface was around 1.0. Such a criterion is demanded to accurately capture interfacial dynamics. These equations are solved using a segregated SIMPLE-C, solver using numerics that are second-order accurate in space, and first-order accurate in time. Note that the lower-order time accuracy is offset by the implicit multi-stepping in the segregated VOF solver, described in Equations 5 - 6.

1. Solidification Model

Solidification is captured in the CMAS using an approach that couples to the VOF method. Within the CMAS VOF phase, there is a solid-coloring function, α_s^*, given as

$$\alpha_s^* = \begin{cases} 1 & T^* < 0 \\ f(T^*) & 0 < T^* < 1 \\ 0 & 1 < T^* \end{cases}, \tag{7}$$

where

$$T^* = \frac{T - T_{solidus}}{T_{liquidus} - T_{solidus}}. \tag{8}$$

In this effort, the latent heat of fusion, h_{fusion}, is important to consider and is captured through

$$h_{is}^* = h_{is} + (1 - \alpha_s^*)\, h_{fusion} \tag{9}$$

Such a model ensures that energy associated with phase-change effects are accounted for. Beyond this, a "flow-stop submodel" is employed to stop the fluid flow in the cells that have reached a particular solid threshold (the flowability threshold, FT). Specifically, when the solid volume fraction from Equations 7 - 9 reaches the FT, the velocity in that cell is set to zero. In order to maintain numerical stability in the solution of the continuity equation, the density in the stopped cells must be held constant, which is achieved with the flow-stop mass compensation option. For the numerical studies in this work, the flow-stop submodel was turned off, except for the solidification characterization in Section III E, where it was varied.

2. Geometry, Mesh, and Boundary Conditions

In this study, several different microstructures (shown in Fig. 2) are evaluated to represent the micro-scale pores. Firstly, a rectangular micro-channel, represented by a two-dimensional (2D) plane extending infinitely into the z-direction. The rectangular channel's purpose is to serve as a benchmark; a case that allows the numerical methods in this model to be compared to analytical models for capillary flow.

This rectangular geometry was evaluated against the results from a feathery micro-channel. This feathery micro-channel was scanned by DLR scientists[4] and a representation of the geometry was converted into a 2D and three-dimensional (3D) geometry, shown in Fig. 2. The 3D geometry is just the 2D geometry extended into the page. Here, the feathery pattern shown on the right is repeated downward until the TBC column is 200 μm deep. This is half the depth of the TBC sample used in experiments[23]. It should be noted that a typical TBC coating on an aircraft component is $\approx 150-180$ μm deep. The TBC coating used in the experiments was larger in order to perform longer kinetic experiments.

The geometry is then meshed using an unstructured trimmed-cell mesh which can be seen in Fig. 3. The 3D simulations used adaptive mesh-refinement (AMR) at the air-CMAS interface.

Due to limitations in the 2D model, a separate set of boundary conditions had to be used in the 2D and 3D models. The 2D model is not capable of spontaneously producing capillary flow, unlike the 3D model. The interface resolution, paired with the lack of a inflow/outflow boundary in the z-direction causes the inertial forces to dominate the flow in the 2D model. So, the flow in the 2D model must be "jump-started" by an enforced pressure gradient. The boundary conditions for the 2D model are summarized in Table I.

Boundary conditions and domain dimensions for the 3D model are summarized in Fig. 2b and Table II. Note that only the feathery geometry was simulated in 3D. All flow boundary conditions are zero-gradient, that is, pressure and volume fraction on each of the boundaries is the same as the fluid entering/leaving the boundary. These boundary conditions are important because they ensure the flow of the CMAS is purely driven by capillary effects and not pressure gradients. While it could potentially make more sense to use engine operating pressures for the simulation's reference pressure, this domain was set up to be more in line with experiments conducted by Naraparaju et al.[6,14,23] to ensure the comparison to experimental data is as accurate as possible.

For both the 2D and 3D geometries, conjugate heat transfer was considered by setting the TBC as a solid region, the walls of the TBC were prescribed as a temperature gradient, (i.e. ΔT_x), of -1 $K/\mu m$, such that the top of the coating is close to a typical operating temperature for an engine environment. The gradient is defined this way to relate the simulation to the TBC sample that was used in experiments[23], which was around 400 μm deep, and manages to be around 400 K cooler at the bottom of the TBC than the top, such that the operating temperature is below the melting point of the materials used. It should be noted there is only a gradient in the x-direction, so any walls on the same x-plane will have a constant temperature, and any walls along the same y-plane will have a temperature that varies.

The wall contact angle of the CMAS phase is expected to be somewhere between 40 and 70 degrees based on experiments[23]. These values are temperature dependent though. For simplicity, a constant wall contact angle of 67 degrees was used[23].

The thermal gradient described above for the boundary conditions was also used as the initial temperature condition for both the fluid region and solid region. The fluid domain's initial velocity was set such that there was a very small downward velocity. This is done because it helps with convergence in the first calculations in the simulation. An additional assumption made in the CFD is that TBC walls are perfectly smooth, which is not necessarily the case in an actual TBC. Gravity was also enabled to capture any infiltration effects from buoyancy. Turning on gravity also adds the Boussinesq Approximation to the energy equation to account for natural convection. However, the effects of natural convection do not dominate the flow.

TABLE I: Summary of labeled boundary conditions for the 2D domain (pressure values with respect to reference pressure $P_{ref} = 101325$ Pa)

Label	Type	Boundary Condition	Value (Units)
1	Inlet	Pressure	3.0 MPa
-	-	Temperature	1530 K
2	Inlet	Pressure	3.0 MPa
-	-	$T(x)$	1530 -$\Delta T_x \times x$ (x in μm)
3	Symmetry	-	-
4	Outlet	Pressure	-50 MPa
-	-	Temperature	1324 K
5	Walls	$T(x)$	1530 -$\Delta T_x \times x$ (x in μm)

TABLE II: Summary of labeled boundary conditions for the 3D domain (pressure values with respect to reference pressure $P_{ref} = 101325$ Pa). Note that the 3D domain is the same as the 2D domain shown in 2b, but extended in the -Z and +Z directions (into and out of the page). The -Z and +Z boundary conditions are unlaballed, but are shown in this table.

Label	Type	Boundary Condition	Value (Units)
1	Inflow/Outflow	$\frac{\partial P}{\partial x}$	0
-	-	Temperature	1530 K
2	Inflow/Outflow	$\frac{\partial P}{\partial x}$	0
-	-	$T(x)$	1530 -$\Delta T_x \times x$ (x in μm)
3	Symmetry	-	-
4	Inflow/Outflow	$\frac{\partial P}{\partial x}$	0
-	-	Temperature	1324 K
5	Walls	$T(x)$	1530 -$\Delta T_x \times x$ (x in μm)
-Z and +Z	Inflow/Outflow	$\frac{\partial P}{\partial x}$	0

Additionally, due to the 2D model assumptions and incompressible air phase, air pockets within the feather gaps de-

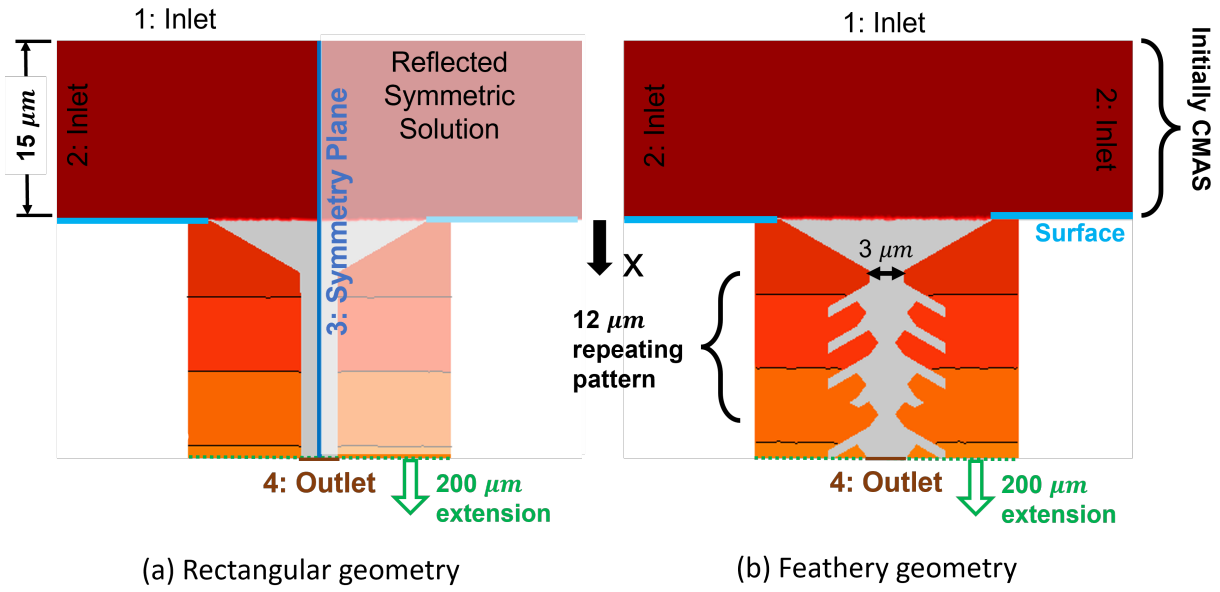

FIG. 2: Dimensions and boundary conditions applied to two channel types. The contours indicate the thermal boundary conditions in the solid. The dark-red colored area is filled with CMAS which infiltrates into the gray region (air). The red-to-orange gradient represents the decreasing temperature within the TBC as depth increases.

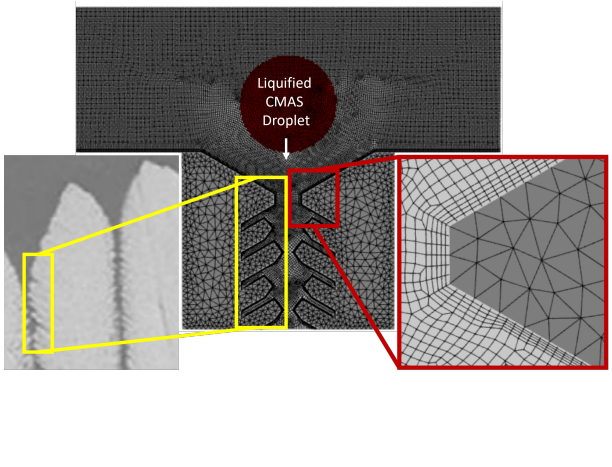

FIG. 3: Overall computational mesh and domain compared to a scanning electron microscope (SEM) image (yellow). The mesh has zoomed-in view in the near-wall region. Also, the feather shape can be correlated to feathers from the SEM image.

manded paths to escape. To accomplish this, the fluid-solid interface was modeled as a porous boundary to allow the air to escape. The boundary was modeled with a pressure rise calculated as

$$\Delta P = -\rho(\alpha|v_n| + \beta)v_n. \tag{10}$$

Here, the values of the external pressure (ΔP), inertial resistance (α), and viscous resistance (β), were set to the ambient pressure (i.e., $0Pa$), 100 (dimensionless), and $1\frac{m}{s}$, respectively. With this model, the air can escape the pore based on the local pressure and is limited to a maximum velocity of $0.01\frac{m}{s}$ according to Eq. 10.

B. Theoretical Model: FPNM

This works also seeks a more representative, but still intuitive way of describing the flow within the feathery microstructure of a TBC. Therefore, a feathery-pipe-network model (FPNM) is formulated and proposed and is based on considering a network of capillary channels. This model was inspired by a capillary flow electrical circuit analogy[30]. However, the circuit analogy does not allow for configurations matching the TBC gap. So, FPNM is proposed. Theoretical model development has also shown that the Lucas-Washburn equation can indeed be extended into larger, heterogeneous porous media[25,31], but this theoretical model is also more generalized and is difficult to specifically model the configurations seen in Figures 1 and 2. In FPNM, there is a primary channel, with other secondary channels extending (almost) perpendicular from the primary tube. In the context of the FPNM, these secondary channels, effectively retard the primary-channel flow. The FPNM model formulation demands added input using the following variables (which can be referenced in Fig. 4:

- n, the number of secondary channels affecting the flow in the primary channel (increases as depth of CMAS in primary tube increases)
- h_p, the depth of the CMAS in the primary channel

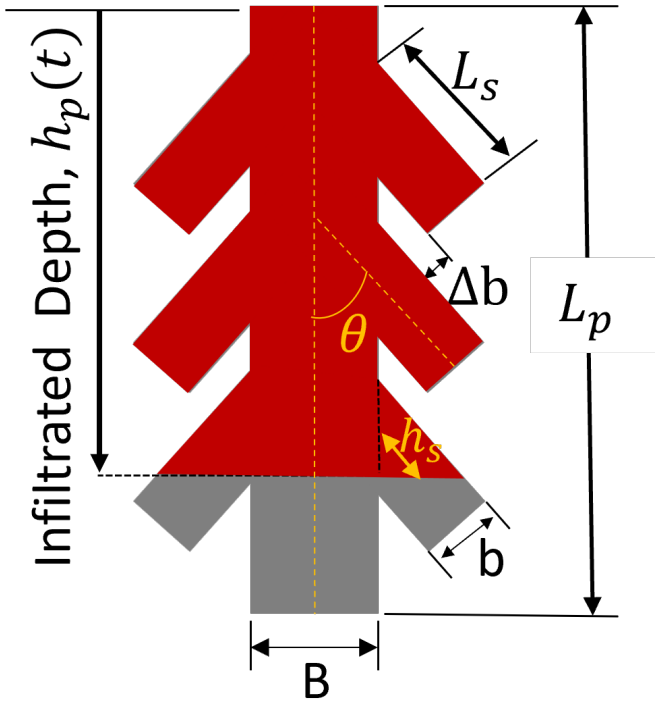

FIG. 4: Visual representation of geometric parameters describing FPNM

- h_s, the depth of the CMAS in a secondary channel
- B is the inter-columnar gap (width of the primary channel)
- b is the feather gap width
- Δb is the separation between each feather gap
- θ is the feather angle
- L_s and L_p are the lengths of the primary channel (the coating depth), and the feather length respectively

A visual representation of these variables is shown in Fig. 4. It is proposed to adapt these variables into the Washburn model[32], which is given as

$$\frac{dh}{dt} = \frac{d^2}{\mu}\frac{\Delta P}{L}. \tag{11}$$

Where $\Delta P = \sigma/d$, this is the proposed relation for the primary channel, as so

$$\frac{dh_p}{dt} = \frac{B^2}{\mu}\frac{\Delta P}{L_p}. \tag{12}$$

However, an additional term to account for the flow in the secondary channels must be added (i.e. the flow that is causing "resistance" in the primary channel). If we assume that this resistance, R_s, takes the form

$$R_s = \frac{b^2}{\mu}\frac{\Delta P}{L_s}cos\theta, \tag{13}$$

it can be said that

$$\frac{dh_p}{dt} = \frac{B^2}{\mu}\frac{\Delta P}{L_p} - ncos\theta\frac{b^2}{\mu}\frac{\Delta P}{L_s}. \tag{14}$$

The number of feathers affecting the flow in the primary channel (n) increases as the depth of CMAS in the primary channel increases. However, n can be solved directly since the primary channel height (h_p), feather width (b), and feather gap width (Δb) are known.

$$n = 2\frac{h_p}{b+\Delta b}. \tag{15}$$

So the overall equation becomes, after substituting $\Delta P = \sigma/d$,

$$\frac{dh_p}{dt} = \frac{B\sigma}{h_p\mu} - 2cos\theta\left(\frac{h_p}{b+\Delta b}\right)\frac{b\sigma}{L_s\mu}. \tag{16}$$

Now, it is assumed that the time it takes for the flow to infiltrate the feathers, $L_s(t)$ is much smaller than the time scale of the primary flow. So, $L_s(t)$ can be integrated with respect to time to get

$$L_s(t) = \sqrt{\frac{\sigma t b}{\mu}}. \tag{17}$$

Implementing this definition and rearranging yields a time-dependent differential equation

$$\frac{dh_p}{dt} = \frac{\sigma B}{\mu}\frac{1}{h_p(t)} - 2cos\theta h_p(t)\left(\frac{1}{b+\Delta b}\right)\sqrt{\frac{\sigma b}{\mu t}} \tag{18}$$

which can be rearranged and rewritten in terms of the Oh with respect to the primary channel, as well as non-dimensional variables $h_p^* = h_p/B$, and $t^* = t/t_B$, where $t_B = \sqrt{\frac{\rho B^3}{\sigma}}$

$$h_p^*(t^*)\frac{dh_p^*}{dt^*} + 2cos\theta\sqrt{\frac{\rho B^3}{\sigma}}\left(\frac{1}{b+\Delta b}\right)\left(h_p^*(t^*)\right)^2 + \sqrt{\frac{\sigma b}{\mu B^2}}\frac{1}{\sqrt{t^*}}h_p^*(t^*) = Oh_B^{-1}. \tag{19}$$

Here, we have a nonlinear, first-order ODE that is readily solvable. To account for non-linear variations of fluid properties, such as viscosity, Eq. 19 is solved in small time increments, and the properties are updated after each increment. Importantly, the maximum viscosity is limited to the viscosity the CMAS achieves at its solidification temperature. Viscosity does not change above this point in FPNM.

C. TBC and CMAS Material Properties

The material properties of both the CMAS and the TBC affect infiltration. Some of these properties are widely documented, such as thermal conductivity of the TBC[33]. Table III shows the properties used for both the CMAS and the TBC. Blank entries are properties not relevant to the model (in this case, for the solid TBC region). Importantly, silicate melts tend to obey Hooke's Law and behave like a viscoelastic material[34].Thus, CMAS is considered an incompressible, Newtonian fluid[6,23,34]. While an equation-of-state has been implemented for CMAS in previous numerical efforts[4], the density variation was found to be incredibly small. Thus, constant density is assumed. Another key departure from Kabir and Sirigiri's work[4,18] is the implementation of temperature-dependent properties in both the CMAS and TBC, as seen in Table III. Particularly, the temperature-dependent viscosity of CMAS would greatly affect the flow kinetics because of the thermal gradient imposed at the outer boundary of the TBC. Capillary flow in microchannels is greatly dependent on viscosity[32], so the rheological properties of CMAS, particularly viscosity, will affect the flow solution. At lower temperatures, the viscosity will be higher, and thus the infiltration will be slower. Higher temperatures lead to less viscous CMAS and faster infiltration. To account for this, the viscosity is modeled as a polynomial from experimental measurements[23] and is implemented as a nonlinear solution step in the CFD solver.

TABLE III: Summary of thermal and physical properties of CMAS and TBC

Property	CMAS	TBC
Thermal Conductivity (W/m-K)	1.15[35]	tabular[33]
Specific Heat (J/kg-K)	900[7]	tabular[33]
Density (kg/m^3)	2690[36]	4800[37]
Dynamic Viscosity (Pa-s)	Polynomial[23]	-
Latent Heat of Fusion (MJ/kg)	19.73[13]	-
Surface Tension (N/m)	0.4[38]	-
Solidus Temperature (K)	1503[14]	-
Liquidus Temperature (K)	1523[14]	-

III. RESULTS AND DISCUSSION

Here, the results from the simulations and analytical models are discussed, starting with a mesh sensitivity study, moving on to comparing the analytical models with the numerical results, and finally characterization based on several properties is considered.

A. CFD Model

1. Benchmark: Capillary Rise in a Circular Tube

Since CMAS infiltration in a TBC is a capillary-dominated flow, the methodology above must be validated for use with such flows. A canonical configuration for a capillary-driven flow is the transient capillary rise in a circular tube. This case is typically used when validating multiphase numerical methods[39,40]. To do this, a 3D cylindrical tube was set up using the same methods described in Section II. Constant viscosity water with no solidification model was used in place of the molten CMAS, and the domain was isothermal. The tube's dimensions and boundary conditions are shown in Fig.5. Zero pressure gradient boundaries were used to ensure only capillary forces are driving the flow. Only water was allowed to enter the tube, while water and air can exit the tube.

Fig. 6 shows the volume fraction of water throughout the capillary rise simulation. Here, a meniscus spontaneously forms due to the capillary action at the tube wall. Then, the meniscus continues to ascend. The ascent rate of the meniscus according to an analytical formulation of the Lucas-Washburn equation[41] should be around 0.32 m/s (Note that this value was achieved ignoring effects of dynamic contact angle, as this phenomenon is ignored in the present study). The ascent rate of the meniscus in this benchmark CFD model is around 0.36 m/s. A 12.5% error is achieved between the analytical Lucas-Washburn equation and the CFD model. The qualitative observations in Fig. 6 and the quantitative comparison between the analytical Lucas-Washburn equation and the CFD model demonstrate the ability of the simulation methodology to resolve capillary-driven flow.

2. Validation: Mesh Sensitivity Study

A mesh sensitivity study was conducted where a single CMAS droplet was resolved. The droplet's initial velocity was 0.2 m/s, allowing for quick impingement of the TBC. From there, the droplet infiltrates via capillary action as normal. The setup for this is shown in Fig. 3. The infiltration depth at 0.1 s of physical time was extracted for several levels of refinement. The results in Fig. 7 and Table IV show convergence. Since results vary incredibly little with finer mesh sizes, a mesh with a base size of 1.4×10^{-7} m will be used for further simulations. Performing the formal grid convergence index (GCI) calculations[42,43] shows that the results in Table IV imply oscillatory convergence, because $0 < \varepsilon_{21}/\varepsilon_{32} = 0.004 < 1$, and a GCI of 7.5×10^{-4}.

TABLE IV: Mesh Sensitivity Results from Fig. 7

Representative Mesh Size (m)	Infiltration depth at 0.1 s (m)
2.1×10^{-07}	4.475×10^{-05}
1.4×10^{-07}	3.281×10^{-05}
1.0×10^{-07}	3.232×10^{-05}
7.5×10^{-08}	3.238×10^{-05}

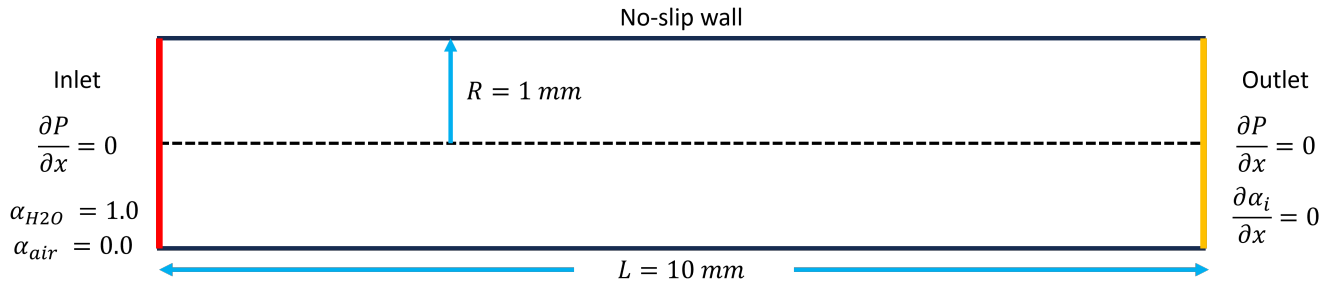

FIG. 5: Diagram showing the dimensions and boundary conditions for the benchmark capillary rise in a tube case.

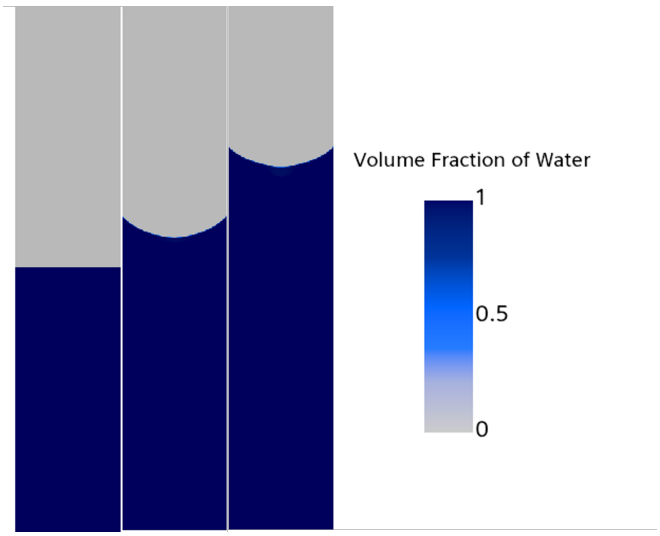

FIG. 6: Simulated capillary flow in a tube at three different stages. From left to right, the flow is initialized halfway up the tube and there is no meniscus. Next, the meniscus spontaneously forms and begins to move upward. Last, the meniscus has moved much further up the tube than where it started. This shows that capillary rise is resolved.

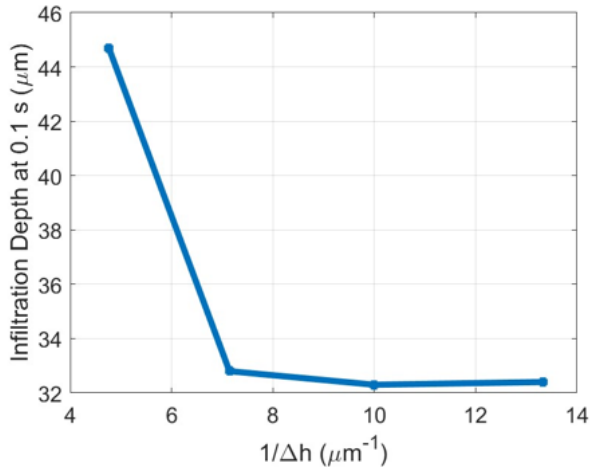

FIG. 7: Infiltration Depth (μm) as a function of the inverse of representative mesh size (μm^{-1})

3. 2D CFD Model

In Section II, it is mentioned that the boundary conditions on the 2D model make it such that it is not strictly a capillary-driven flow, but also inertially-driven. This has unintneded consequences on the results. The limitations in the 2D model causes the flow to reach a state of equilibrium, as seen in Fig. 8. This phenomenon is non-physical, since the CMAS should continue to infiltrate instead of reach a point of equilibrium[6]. So, the 2D geometry cannot be used to "resolve" the infiltration process. However, it is still valuable in the sense that it can demonstrate a microstructure's ability to stop the infiltration under different circumstances.

To understand the effect of geometry, the 2D CFD results from the rectangular and feathery channel geometries are shown in Fig. 2. Additionally, the 2D CFD results are compared to analytical solutions of the open-pipe and concentric-pipe models (OPM, and CPM respectively)[23] based on models detailed in Appendix A. Fig. 8 shows the infiltration depth versus time for the rectangular and feathery simulations, co-plotted with the analytical OPM and CPM solutions. Note that the CFD results in Fig. 8 account for a fluidic viscosity that varies with temperature which is based on polynomial fit to experimentally-measured data[6].

First, consider the rectangular and feathery CFD data in Fig. 8. These CFD results show that the feathery channel works to mitigate infiltration as compared to the rectangular channel. Such an inference can be drawn from the CMAS infiltrating to shallower depths for the feathery channel compared to the rectangular channel.

To understand the evolution of CMAS attack, the time history of the CMAS distribution is discussed. The effort starts with data extracted from the CFD results. The CFD time history is plotted in Fig. 8 and, at several points of interest in time, contour plots of the CMAS volume fraction and TBC temperature are plotted in Fig. 9. In the contour plots, the red/gray area shows the distribution of air and CMAS, and the red-orange gradient shows the temperature distribution within the TBC (with isocontours in intervals of 1 K). First, consider the initial infiltration in both the rectangular and feathery channels on a time interval from $t = 0$ to $t = 0.001s$ in Fig. 8. This early infiltration occurs much faster and the rate of infiltration appears to significantly slow down thereafter. Such an

fast infiltration occurring early is a result of the conical shape of the micro structure in the coating, shown in Fig. 9. It appears to work much like a converging nozzles, where the flow accelerates with the reduction of the cross-sectional, interstitial area.

Now consider a later time interval range from $t = 0.001 - 0.13s$ in Fig. 9. At $t \approx 0.05s$, the infiltration rates of the rectangular and feathery channels diverge. There, the infiltration in the rectangular channel continues at a faster rate than in the feathery channel. At $t \approx 0.13s$, the CMAS in the feathery channel reaches an equilibrium state and no longer infiltrates. Concurrently, the infiltration in the rectangular channel shows a trend that indicates it begins to slow down. Lastly, after $t \approx 0.15s$, the infiltration in the rectangular channel eventually reaches an equilibrium as well. It is important to emphasize that the infiltration in the feathery channel reaches an equilibrium faster and penetrates to shallower depths than in the rectangular channel. Such an observation is consistent with previous experimental results[6] and further demonstrates the effectiveness of feathery TBCs to resisting CMAS attack.

In further evaluation of the results, it can be observed from Fig. 9 when focusing on the distribution of air and CMAS that air pockets form within the infiltrated CMAS. With respect to this, recall that the the thermal conductivity of air is $1-2$ orders of magnitude lower than that of the TBC and CMAS (depending on the temperature). Such air pockets can also not support convection. Hence, the air pockets potentially contribute to a decrease of thermal conductivity in a TBC that has experienced CMAS attack.

In Fig. 9(center) and 10(center), a developing temperature profile is seen within the TBC. The temperature profile develops as energy is absorbed by the CMAS moving downward and that energy is conducted back into the TBC. In Fig. 9(right), after further infiltration, the temperature profile switches directions along the TBC interface. This happens because more energy is being redirected to satisfy the latent heat of fusion of CMAS. The CMAS is effectively cooling the TBC. This effect is less drastic in Fig. 10 because there is overall less infiltrated CMAS available for energy absorption.

One discrepancy between these results and previous work is that the meniscus of the CMAS/air interface is convex in Figures 9 and 10. Previous work suggests that this meniscus should be concave[23]. This discrepancy is likely caused by the initial condition in the CFD simulation. That is, the flow is driven by a pressure gradient and capillary action, as opposed to being driven by capillary action from the start. Another discrepancy between experiments, analytical models, and 2D CFD is that the CMAS in the 2D CFD model reaches a state of equilibrium, rather than continuing to infiltrate. This limitation could be fixed with more mesh resolution at the CMAS/Air interface so that the capillary action is properly resolved, but the numerical methods being used here do not support AMR in 2D simulations. Hence, a 3D model is necessary to properly resolve the capillary-driven part of this phenomenon.

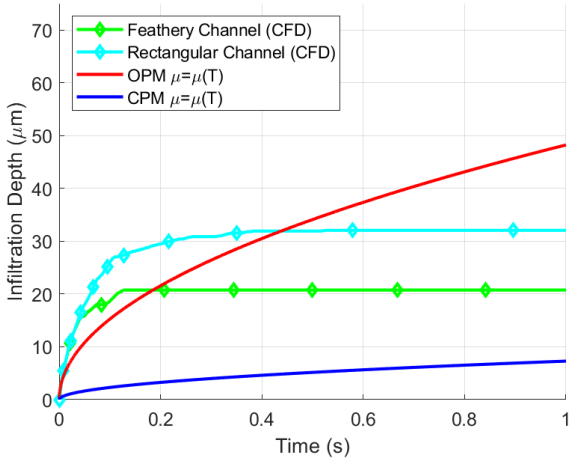

FIG. 8: Comparison of infiltration depth versus time for the 2D CFD model's rectangular and feathery micro-channels co-plotted with the analytical pipe model results. Note that the feathery channel reaches an equilibrium at shallower depths at a shorter time than the rectangular channel.

4. 3D CFD Model

While the 2D model was unable to attain spontaneous capillary flow, the CMAS in the 3D model was able to spontaneously form a meniscus, and infiltrate the TBC without the assistance from an external pressure gradient. Hence, this model can reasonably resolve the actual physical processes in the CMAS infiltration, rather than just a comparison tool like the 2D model.

The infiltration depth as a function of time for the 3D model is shown in Fig. 11. The reults from the 3D model, 2D models, OPM, and CPM are compared. Fig. 11 shows that the CMAS in the 3D CFD model does not reach a point of equilibirum, as the 2D CFD does, and the shape of the infiltration versus time curve is similar to that of OPM and CPM.

The time resolution of experimental measurements is very low, with measurements taking place every few minutes during infiltration[6]. The first data point that can be compared to is taken at 120 s. One drawback of the 3D CFD model is the time it takes to run. Even on an HPC system using 4 Intel Xeon Platinum 8558 processors (192 compute cores), it still takes nearly a week to run the 3D CFD model to 0.1 s of physical time. As a result of this, to compare to experiments, the 3D CFD infiltration versus time data must be fitted to a curve, and the depth at 120 s must be extrapolated to compare to the experiments. The fitted curve is shown in Fig. 11, and the extrapolated depth at 120 s is shown in Table V. Note that the time-period where the meniscus was forming was excluded from the curve-fit. The extrapolated depth of the 3D CFD model at 120 s is $50\ \mu m$. So, the 3D CFD model underpredicts the infiltration depth compared to all other models. This under-prediction can be partially explained by the

Importantly, the prediction from the extrapolated curve is in between the results from OPM and CPM in Fig. 11. Experi-

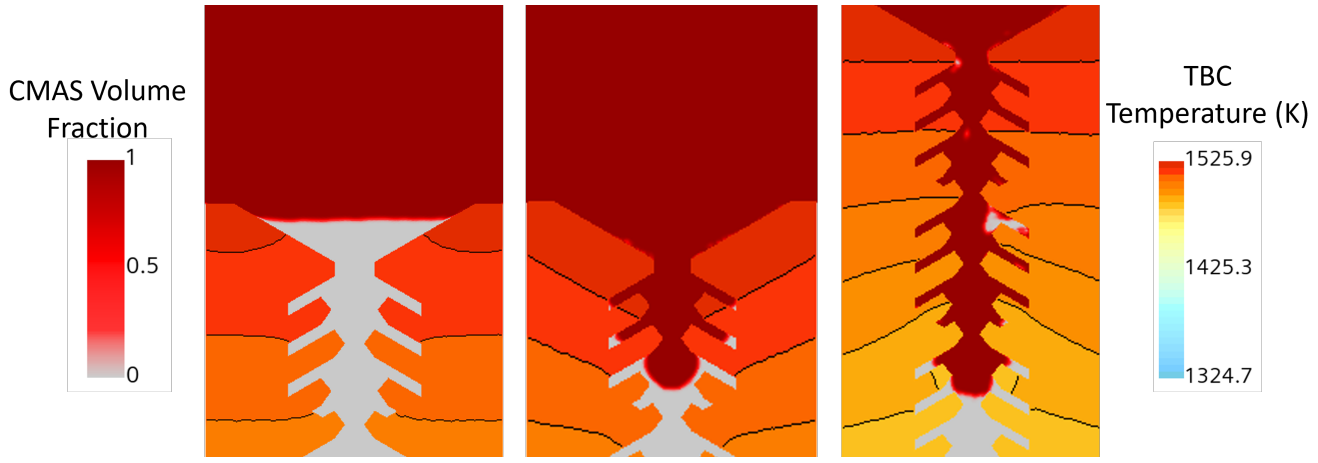

FIG. 9: Time history of the feathery TBC simulation showing the volume fraction of CMAS and the temperature of the TBC (for $Oh_{initial} \approx 115$ to $Oh_{final} \approx 1300$). The left ($t \approx 2 \times 10^{-5} s$) image shows the initial conical infiltration, the middle image ($t \approx 0.005 s$) shows CMAS as it infiltrates the feather arms, and the right image ($t \approx 0.13 s$) is the equilibrium point. Note that the isolines in the TBC represent the thermal gradient, where the temperature at each isoline is 1 K less than the one above it.

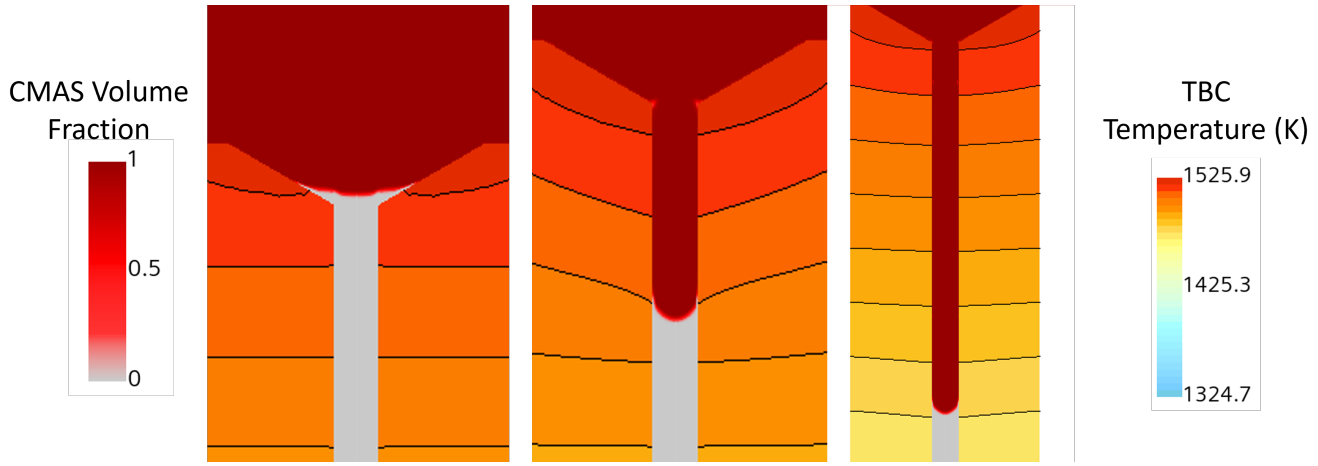

FIG. 10: Time history of the rectangular TBC simulation showing the volume fraction of CMAS and the temperature of the TBC (for $Oh_{initial} \approx 115$ to $Oh_{final} \approx 1300$). The left image ($t \approx 1 \times 10^{-5} s$) shows the initial conical infiltration, the middle image ($t \approx 0.1 s$)shows CMAS as it infiltrates the thin rectangular channel, and the right image ($t \approx 0.4 s$) is the equilibrium point. Note that the isolines in the TBC represent the thermal gradient, where the temperature at each isoline is 1 K less than the one above it.

mental measurements at 120 s are also between the predictions for OPM and CPM[6]. So, the 3D CFD model is more closely aligned with experimental results than the present theoretical models. This is beneficial because it allows more accurate predictions, but since the 3D CFD model is so computationally expensive, it is worth looking for a simpler model, such as FPNM. However, this is only the case at small time scales. At larger timescales, the 3D CFD model under-predicts the infiltration, as seen in Table V.

Fig. 12 shows images of the CMAS infiltration at several important time points. Fig. 12 (left) shows the meniscus spontaneously forming, and the CMAS beginning to move downward from its original state. Then, Fig. 12 (center) shows the CMAS starting to enter the feather gaps as it creeps along the TBC walls. Interestingly, in Fig. 11, there are brief pauses in the infiltration (like between $t = 0.015 s and t = 0.0175 s$). These pauses seem to correlate periods where the flow in the primary gap stops, but the flow in the feather gaps continues. The flow must reach a certain point in the feather gap for the CMAS to continue to infiltrate the primary channel. This phenomena occurs between the timepoints in Fig. 12 (center) and Fig. 12 (right).

B. FPNM: Benchmarks with CFD, Conventional Models, and Experiment

Consider infiltration comparisons of the newly formulated FPNM model to results from the OPM, CPM, and the CFD models. Results are plotted in Fig. 13, with comparisons of

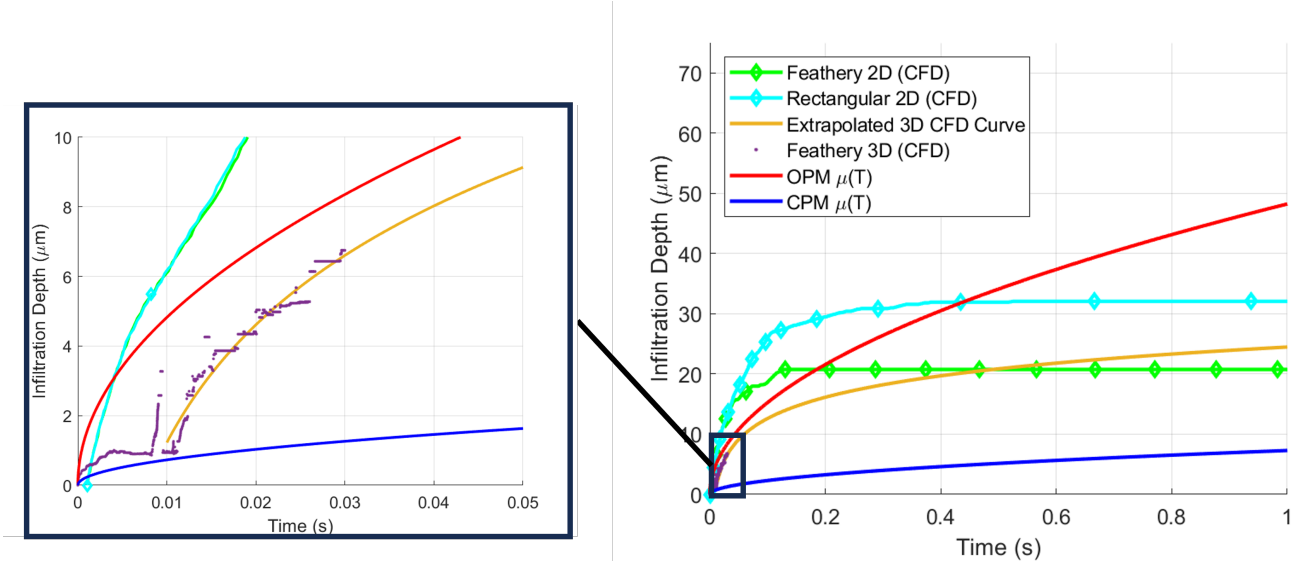

FIG. 11: Infiltration depth versus time for the 3D CFD model. Here, the simulation data is plotted along with a curve-fit of that data in order to extrapolate past the simulated time.

FIG. 12: Time history of the feathery 3D CFD model showing the volume fraction of CMAS and the temperature of the TBC. The left image ($t \approx 1 \times 10^{-3} s$) shows the initial infiltration, where the meniscus begins to spontaneously form, the middle image ($t \approx 0.12 s$) shows the CMAS as it begins to enter the first feather gap, and the right image ($t \approx 0.035 s$) shows the CMAS as fully infiltrating the feather arms, and continuing to move down the TBC. Note that the isolines in the TBC represent the thermal gradient, where the temperature at each isoline is 1 K less than the one above it.

FPNM (Eq. 18), OPM (Eq. A2), and CPM (Eq. A3). The CFD results are based on the model described in Fig. 8. The FPNM infiltration was calculated with both constant viscosity ($\mu = 5.65$ Pa·s) and temperature-dependent viscosity, while OPM and CPM were only calculated with constant viscosity. In the early stages of this comparison ($t < 0.025 s$), it can be observed that the FPNM provides an improved correlation with the CFD results compared to the OPM and CPM models. The improved agreement is observed in the initially rapid infiltration rate from the FPNM. As time evolves to $t \approx 0.5 s$, the FPNM tends to be more in-line with OPM and CPM. The CFD model results shows an equilibrium infiltration depth, whereas the FPNM, OPM, and CPM results indicate that equilibrium is not achieved. Additionally, at times beyond $0.5 s$, the FPNM also appears to be bounded by the OPM and CPM results. To summarize the results, the three model results at $120 s$, and a measured experimental result are summarized in Table V. The CFD results are not included in this table because the infiltration equilibrates in the CFD, so the results are not directly comparable. Table V shows that the experimentally measured infiltration is also bounded between OPM and CPM. However, FPNM is closer to the experimental result than OPM. Thus, the results demonstrate that the FPNM enhances the predictions of infiltration depth for CMAS attack.

One aspect the FPNM does not take into account is the solidification of the CMAS. As the CMAS approaches the so-

lidification onset temperature, it will tend to slow down not just due to an increase in viscosity, but because the CMAS itself will begin to crystallize[23]. This process occurs beyond what is calculated in Fig.13 for FPNM, OPM, and CPM. However, this shows that FPNM is over-predicting the infiltration depth. If a solidification model were included in FPNM, it would align even closer to experimental results.

Another advantage of the FPNM is its computational efficiency. While it is not as efficient as a purely algebraic model, like OPM or CPM, it is far more efficient than a fully-fledged CFD model. The computational time required to solve the FPNM equation is on the order of minutes whereas the CFD models could take hours for a 2D model or days for a 3D model. Thus, the FPNM is a compromise between the speed of OPM/CPM, and the accuracy of CFD. The speed of FPNM also allows for quick evaluation of different material properties. The ability to solve FPNM incrementally also allows the addition of additional non-linear steps to the solver, such as solidification, or other temperature-dependent properties. The speed of FPNM could be further optimized using parallelization.

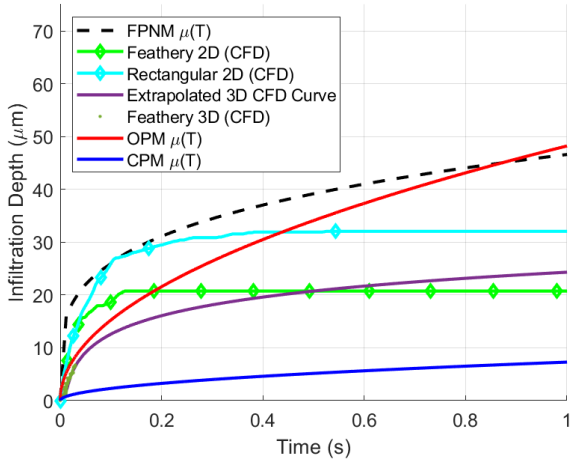

FIG. 13: Depth versus time for the CFD, analytical pipe models, and the proposed FPNM (with both a constant viscosity and temperature-varying viscosity solution).

TABLE V: Infiltration depth at 120 s from experiments[23], open-pipe[23], concentric-pipe[23], and feathery pipe network model

	Infiltration Depth (μm)
Experiment	125
Open-pipe	176
Concentric-pipe	95
Feathery Pipe-Network Model	154
3D CFD Model	50

C. Geometric Parameterization with FPNM

The quick solutions offered by FPNM (the ODE can be solved in minutes, whereas CFD can take hours or days) allows for easy manipulation of geometric parameters without the need to change a physical model, remesh, and rerun the solution every time. Hence, it is advantageous to use FPNM to study how the geometric parameters of the TBC affect the CMAS infiltration.

First, the affect of the intercolumnar gap, B, was analyzed, and the results are shown in Fig. 14. Here, it is shown that larger intercolumnar gaps lead to faster infiltration, and this effect scales nonlinearly, meaning larger gaps allow exponentially faster infiltration. This data is supported by other's numerical efforts evaluating the TBC microstructure[4]. A good analogy to describe why this physically makes sense is blood flow. When arterioles and venules bifurcate and becomes smaller, their flow-resistance becomes larger, because the resistance is inversely proportional to R^4[44]. So, it can be said that smaller intercolumnar gaps increase the TBC's resistance to infiltration.

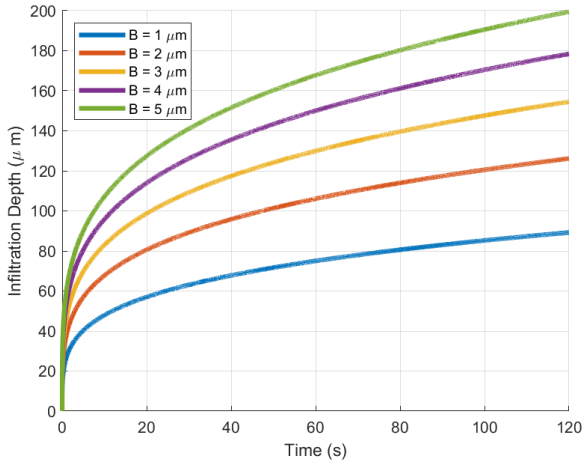

FIG. 14: Depth versus time for various intercolumnar gap widths using FPNM.

Similarly, the feather gap width, b, was evaluated, and results are shown in Fig. 15. Here, larger feather gaps lead to faster overall infiltration in the primary channel, because the CMAS must fully infiltrate the feather gaps before it can move further down the primary channel. Hence, increasing the flow resistance at the feather gap increases the overall resistance. However, decreasing the feather gap width had diminishing returns, after $b = 2\mu m$, the infiltration is not mitigated nearly as much as before $b = 2\mu m$.

The results in Fig. 14 and Fig. 15 elucidate an important ratio, $B^* = B/b$. As B^* increases, the infiltration will become slower. Designing TBC microstructures around this ratio will lead to more effective infiltration mitigation.

The feather angle can also influence the infiltration characteristics. Infiltration depth versus time for several feather angles are shown in Fig. 16. It is shown that larger feather an-

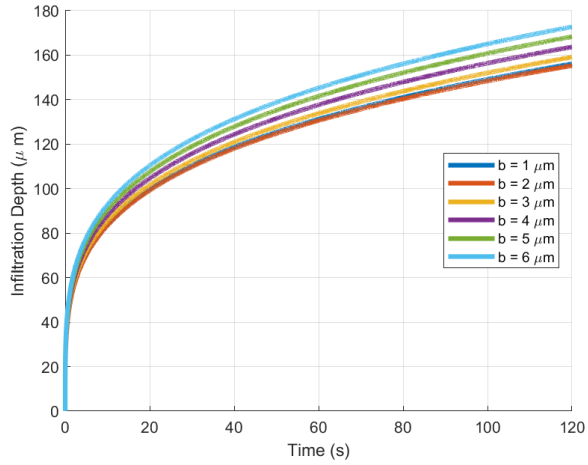

FIG. 15: Depth versus time for various feather gap widths widths using FPNM.

gles tend to increase the infiltration speed, while smaller angles decrease the infiltration speed. However, increasing the feather angle has a greater effect than decreasing it.

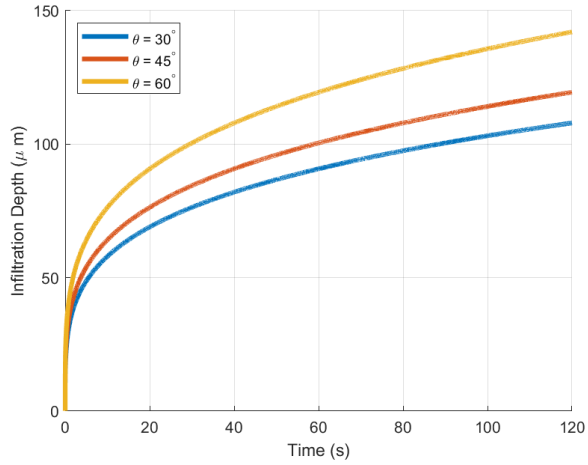

FIG. 16: Depth versus time for various feather angles widths using FPNM.

D. Characterization Based on Ohnesorge Number with CFD and FPNM

In an effort to better understand micro-scale flows, we look at a more generalized fluid flow in the microstructures shown in Fig. 2. We are particularly interested in whether bringing the feathery microstructure into the broader world of microfluidics has any desirable effects. For this effort, the effect of viscosity and surface tension are evaluated. These are captured in the Ohnesorge Number, (Oh), a dimensionless number that represents the ratio of the viscous forces to the inertial and interfacial forces ($Oh = \mu/\sqrt{\rho\sigma L}$). The rectangular and feathery micro-channel simulations were reevaluated, replacing the experimentally measured viscosity with a constant viscosity, while the surface tension was held constant. Similarly, different Oh were used as inputs for FPNM. Note that constant viscosity would not be a great assumption for the CMAS/TBC problem. However, the goal here is to generalize the approach for potential applications outside of CMAS infiltration in TBCs. To provide some context, the CMAS in a simulation with the temperature-dependent viscosity would vary from $Oh \approx 10$ at the initial condition to $Oh \approx 100$ at its maximum depth. So this analysis allows evaluation of materials outside of that range. Hence, a range of Oh were evaluated to understand how Oh affects the infiltration time in the CFD model, and FPNM. Fig. 17 plots the non-dimensional equilibrium point (where $D^* = D/b$, b is the columnar gap width) against infiltration depth for various Oh. An interesting result is that, at lower Oh, the rectangular micro-channel is more effective at inhibiting fluid flow, but around $Oh = 500$, this trend switches, and the feathery microstructure becomes more effective. Additionally, at low Oh, there is also a very high sensitivity to the input Oh. From these studies, we see that the feathery structures are not always most effective and that there are regions where viscosity and surface tension parameters can play a critical role in two-phase flow in different microstructure geometries.

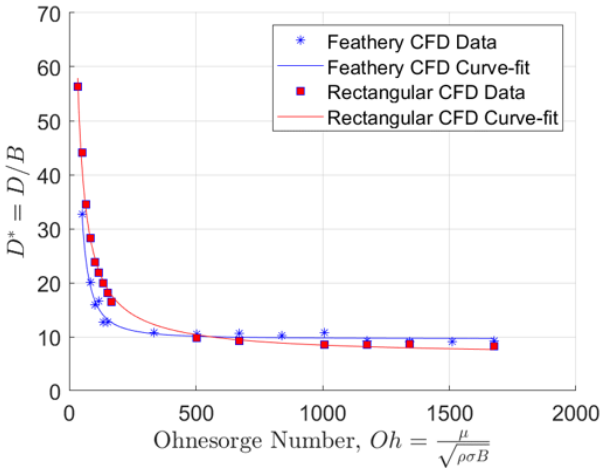

FIG. 17: Non-dimensional equilibrium depth versus Oh for the rectangular and feathery micro-channels using the CFD model. At lower Oh, the feathery microstructure allows the molten liquid to infiltrate further than the rectangular channel. However, around $Oh = 500$, this switches, and the feathery channel is more effective at stopping infiltration.

Fig. 18 shows how the infiltration as a function of time is affected by Oh in FPNM. Here, it is shown that as viscous effects begin to dominate the infiltration process, the liquid tends to infiltrate slower. However, as surface tension dominates the flow, the liquid tends to infiltrate faster. Hence, the viscosity of the liquid acts as a resistive force, impeding infiltration whereas the surface tension acts as a compliant force,

allowing infiltration.

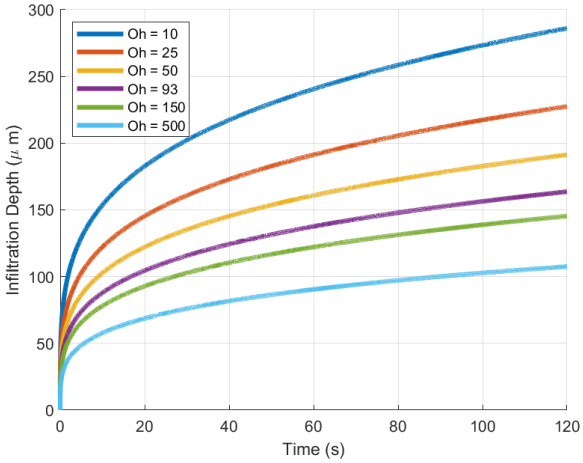

FIG. 18: Infiltration depth versus time with various *Oh*. Constant viscosity FPNM was used for each calculation.

E. Characterization Based on Solidification

The effort now moves to evaluate the effect of solidification on the infiltration time. Such studies are developed using simulations that have an experimentally-measured viscosity (see Table III[6]), which couples to the solidification model described in Eq. 7. In Fig. 19, are extracted the infiltration depth versus time for both the feathery and rectangular channels. To evaluate the sensitivity of the flowability threshold (FT), the parameter was varied in each simulation. and Fig. 19 compares these results to the result without solidification.

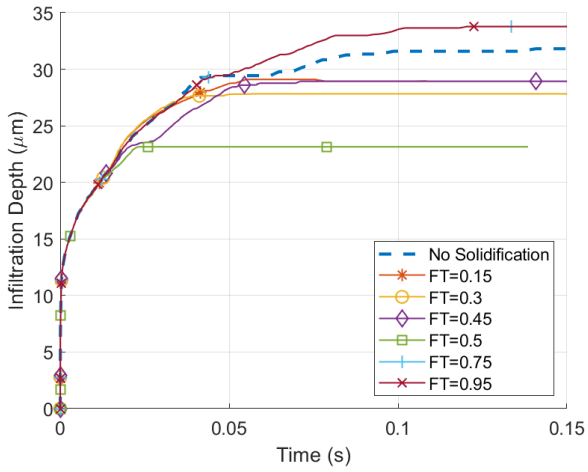

FIG. 19: Infiltration depth versus time for the feathery and rectangular micro-channels with solidification (using a range of flowability thresholds) compared to no solidification.

Further evaluation of Fig. 19 demonstrates the clear character that FT affects both the equilibrium depth and the equilibrium time. The Infiltration with the low FT values (i.e., $FT = 0.015$) tends to behave similarly to infiltration without solidification. Interestingly, as FT increases, the infiltration follows a less clear, non-monotonic pattern. That is, the equilibrium depth for larger FT cases indicated shallower equilibrium infiltration depths as compared to no solidification, but the response does not indicate a monotonic reduction in the depth as FT decreases. For example, the infiltration profile for $FT = 0.75$ and $FT = 0.95$ are very similar. Such overlap suggests that after some threshold is crossed, the result will not change (i.e., the effect is saturated). It is interesting to point out that these cases also have a longer time to equilibrium and equilibrate at the deepest infiltration depths. In general, as the FT value decreases, solidification appears to decrease the infiltration depth. Note that not including solidification may most desirable as it provides a good measure of a conservative, "worst-case scenario" and therefore aims to approximately bound the infiltration depth without input uncertainty associated with FT.

F. Characterization Based on Temperature Gradient

A key property of a TBC is its ability to reduce the temperature between the hot engine flow, and the substrate material. So, TBCs with different temperature gradients between the top and bottom would offer varying degrees of thermal protection. Now, we seek to understand how the temperature gradient in the TBC would affect the degree of CMAS mitigation ability. Both the 3D CFD model and FPNM were evaluated when under temperature gradients, ΔT_x of 0.1, 1, and 10 $K/\mu m$. The results from this are shown in Fig. 20 and Fig. 21

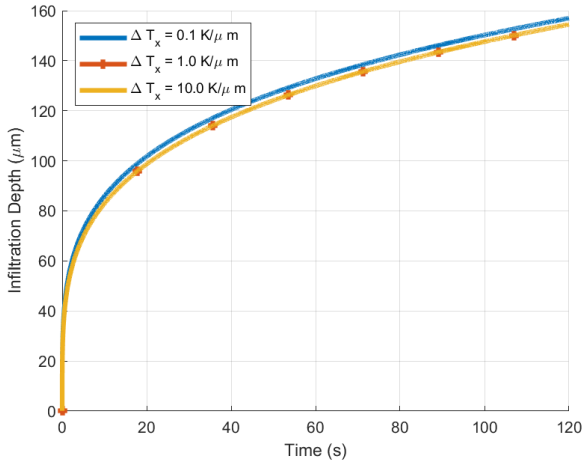

FIG. 20: Infiltration depth versus time for the feathery micro-channels using FPNM. The temperature gradients $\Delta T = -1K/\mu m$ and $\Delta T = -10K/\mu m$ both make the CMAS reach its maximum viscosity (the temperature at which the CMAS is fully solid) very quickly, so the curves overlap.

Fig. 20 shows that less intense temperature gradients in

the TBC lead to somewhat faster infiltration. Beyond a certain point, however, more intense temperature gradients do not lead to less infiltration. This is because maximum viscosity limit imposed on the model. Once the CMAS is considered solidified, the viscosity is no longer changing. So, if the CMAS reaches the solidification viscosity within the first few μm, then the infiltration will remain constant afterward. This is why the curves for $\Delta T_x = 1K/\mu m$ and $\Delta T_x = 10K/\mu m$ overlap in Fig. 20.

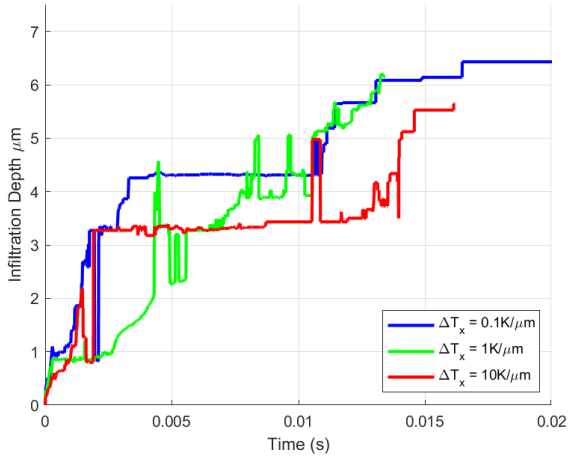

FIG. 21: Infiltration depth versus time under for the feathery micro-channels under various TBC temeprature gradients 0using the 3D CFD model.

Fig. 21 shows results for the same ΔT_x used in Fig. 20, but using the 3D CFD model. Here, the overlap of $\Delta T_x = 1K/\mu m$ and $\Delta T_x = 10K/\mu m$ does not occur. This is likely due to the slightly nonlinear variation of the temperature in the TBC and CMAS. The latent heat of fusion of the CMAS in this model means the CMAS is absorbing different amounts of energy depending on the temperature, so the viscosity of the CMAS at a specific depth in the TBC is not one-to-one between the CFD models and FPNM. Fig. 21, shows that infiltration is dependent on the temperature gradient in the TBC in both directions, unlike the results from FPNM in Fig. 20.

IV. CONCLUSIONS

A method to directly resolve CMAS infiltration in TBCs was formulated and carried out via CFD-based numerical simulations. The study evaluated a 2D rectangular and feathery channel, and a 3D feathery channel using CFD methods. The 2D CFD models failed to resolve spontaneous capillary flow, and had to be driven by a pressure gradient, resulting in infiltration that was partially driven by inertial loads and capillary action. As a result of this, the results from the 2D CFD are non-physical, but can still elucidate important information about the infiltration process. The 3D CFD model was able to resolve spontaneous capillary flow, as indicated by the spontaneous formation of a meniscus, and downward flow occurring without the presence of a pressure gradient.

We then compared infiltration depth CFD predictions for the 2D CFD models using conventional analytical OPM and CPM results (seen in Fig. 8). The CFD results from Fig. 8 showed that the feathery microstructure was better at resisting infiltration, and that the CMAS infiltrated to shallower depths prior to reaching an equilibrium. Interestingly, the equilibrium character observed in CFD was not present in the analytical OPM and CPM models. This was the first indication that the 2D model was not sufficient for resolving capillary flow. It is proposed that the 3D CFD model accounts for this discrepancy by allowing better interface resolution with AMR. The 3D CFD model results, shown in Fig. 11 show that the flow in the 3D CFD model does not reach a state of equilibirum, like the 2D CFD model. The images of the infiltration shown in Fig. 12 shows that a meniscus does spontaneously form, providing evidence that the flow in the 3D CFD model is driven by capillary forces. A drawback of the 3D CFD model is that it is computationally expensive. This was alleviated by running the simulation for less time, and fitting the infiltration depth versus time data to an exponential curve. This resulted in a curve where results were extrapolated at desired time points beyond the simulation time. The extrapolated curve allowed a direct comparison between experiments, analytical models, and the 3D CFD model. The 3D CFD model, when extrapolated to 120 s, predicted a depth that was between the prediction of OPM and CPM. This is important because the experimental measurement at 120 s was also between the predicted results from OPM and CPM. These results are highlighted in Table V. This shows the 3D CFD model is more accurate in predicting cMAS infiltration than OPM and CPM. However, the computational expense demands a simpler model, such as FPNM.

The model of viscosity, its link to thermal conditions and state, are also important to understand. The CFD indicated the presence of air pockets that may contribute to the overall degradation of TBC properties after CMAS attack[6,14,23]. We propose that the degradation at least partially occurs because of the difference in thermal conductivity between the TBC, the CMAS, and the air, which can be 2-3 orders of magnitude depending on the operating conditions.

In this effort, we also developed a novel analytical model referred to as the "Feathery Pipe-network Model" (FPNM). The method is derived on first-principles of capillary flow, and implemented to estimate the infiltration depth as a function of time in a feathery coating. Comparing the result from FPNM to the OPM, CPM, and experimental results showed that FPNM more closely resembled the simulated results at early infiltration times. At later infiltration times, FPNM became bounded between the OPM and CPM. The FPNM result also aligned better with the experimental result, having only a 23% error on the upper bound, as opposed to a 40.8% error for OPM. Therefore, the usage of the FPNM and CPM leads to a path that can potentially enhanced infiltration depth predictions (more accurate than using OPM and CPM) useful for TBC design.

FPNM was then used for several parametric studies. First, the intercolumnar gap, B was varied and Fig. 14 shows that

smaller B leads to less infiltration. This trend was nonlinear, with smaller B leading to exponentially slower infiltraiton. Next, the feather gap width, b, was varied, and Fig. 15 shows that smaller feather gaps leads to slower infiltration. However, this effect had diminishing returns beyond $b = 2\mu m$. Lastly, the feathery angle, θ was varied and Fig. 16 shows that shallower feather angles lead to slower infiltration.

In an attempt to bring expand the discussion into the larger world of microfluidics, the infiltration process was then characterized using 2D CFD and FPNM based on the Ohnesorge Number of the liquid. The Ohnesorge Number was varied by varying the viscosity of CMAS, with all other terms fixed. Results from Fig. 17 show that the 2D rectangular channel column was more effective at stopping infiltration of CMAS with low Oh, and the 2D feathery channel was more effective at stopping infiltration of CMAS with high Oh. FPNM shows that larger Oh tends to cause slower infiltration.

Next, the effect of solidification was considered in the infiltration process via implementing a solidification model in the 2D CFD, where the flowability threshold was varied. Results from these CFD cases produced inconsistent infiltration profiles. No pattern was observed until $FT = 0.75$. For this value and beyond, the infiltration profile was identical. However, none of these results significantly changed the equilibrium depth from the CFD result without solidification. Hence, it is reasonable to account for flow-stoppage purely with viscosity.

Lastly, the effect of the temperature gradient in the TBC was varied. The primary effect of this was that the viscosity would change slower in less intense temperature gradients, and faster in more intense temperature gradients. Hence, the effectiveness of the TBC in preventing heat transfer has a direct impact on its effectiveness in mitigating CMAS infiltration. So, the temperature gradient was varied in both the 3D CFD and FPNM. Fig. 20 and 21 show that less intense temperature gradients lead to faster overall infiltration, and more intense temperature gradients leads to slower infiltration. This happens because viscosity becomes larger faster in the more intense temperature gradient. However, differences between the implementation of the temperature-dependent viscosity in FPNM versus the CFD model mean there are discrepancies in the two models when the same temperature gradients are imposed.

Overall, this work introduces new methods of predicting CMAS infiltration in TBCs. the 3D CFD model leads to more accurate predictions, but is more computationally expensive, and FPNM is less accurate but much faster. FPNM was also used to parameterically evaluate the geometry of the TBC microstructure so that better microstructure design decisions can be made.

There is much future work to consider. A chemical reaction model could be implemented in the CFD to predict where sintering occurs once the phase change happens between the CMAS and TBC. One could also implement a solid stress model in the CFD, which would help predict the delamination process. FPNM could also be improved by accounting for solidification of the CMAS, so that temperature and viscosity aren't only directly correleated with infiltration depth.

ACKNOWLEDGMENTS

- This material is based upon work supported by the National Science Foundation Graduate Research Fellowship under Grant No. GR104853.
- This material is based upon work supported by National Science Foundation grants OISE 1460045, OISE 1952523

CONFLICT OF INTEREST

The authors have no conflicts of interest to disclose

AUTHOR CONTRIBUTIONS

Brendon Cavainolo: Conceptualization (lead); Methodology (lead); Formal Analysis (lead); Validation (lead); Visualization (lead); Writing - original draft (lead); **Ravisankar Naraparaju:** Conceptualization; Methodology; Resources; Supervision (supporting); Writing - review & edit (equal) **Mohammad-Rizviul Kabir:** Conceptualization; Methodology; Resources; Writing - review & edit (equal) **Michael Kinzel:** Supervision (lead); Resources Writing - review & edit (equal)

DATA AVAILABILITY

Data can be made available upon reasonable request to the corresponding author.

Appendix A: Description of open-pipe and concentric-pipe models

A summary of the open-pipe and concentric-pipe models is presented here. For a more in-depth description, please see "Estimation of CMAS Infiltration Depth in EB-PVD TBCs: A New Constraint Model Supported with Experimental Approach"

$$t = \frac{\mu r\, h^2}{2\sigma k cos\theta} \tag{A1}$$

here, t is the infiltration time, r is the radius open for infiltration, h is the infiltration depth, μ,σ, θ are viscosity, surface tension, and contact angle respectively[6,45]. The parameter k represents the porosity and varies depending on whether the open-pipe or concentric-pipe model is being used. Some difficulties arise here, as some of the properties in the above equation vary nonlinearly with temperature, so initial values will be used for the calculations. The open-pipe model defines k as the following

$$k = \frac{r^2\phi^2}{8\tau(1-\phi)^2} \tag{A2}$$

here ϕ is the overall pore fraction, and τ is a geometric factor based on a ratio of area of the column to area of the feather arms, and it was found to be 2.31 for feathery microstructures[23].The concentric-pipe model is similar, but defines k as

$$k = \frac{\phi}{8\tau^2}b^2\left[1+\frac{a^2}{b^2}+\left(1-\frac{a^2}{b^2}\right)\frac{1}{ln(a/b)}\right] \tag{A3}$$

where a and b are the outer radii of the concentric pipes[23].

[1] W. Chen and L. Zhao, "Review – Volcanic Ash and its Influence on Aircraft Engine Components," Procedia Engineering **99**, 795–803 (2015).

[2] J. L. Smialek, "The Chemistry of Saudi Arabian Sand: A Deposition Problem on Helicopter Turbine Airfoils," (1991).

[3] T. D. Bennett and F. Yu, "A Nondestructive Technique for Determining Thermal Properties of Thermal Barrier Coatings," Journal of Applied Physics **97**, 13520 (2005).

[4] A. K. Sirigiri and P. D.-I. W. Kowalczyk, "Modeling and simulation of CMAS infiltration in EB-PVD TBCs," (2018).

[5] A. Flores Renteria and W.A.Kaysser, "A small-angle scattering analysis of the influence of manufacture and thermal induced morpological changes on the thermal conductivity of EB-PVD PYSZ thermal barrier coatings," Fakultät für Georessourcen und Materialtechnik (2007).

[6] R. Naraparaju, M. Hüttermann, U. Schulz, and P. Mechnich, "Tailoring the EB-PVD columnar microstructure to mitigate the infiltration of CMAS in 7YSZ thermal barrier coatings," Journal of the European Ceramic Society **37**, 261–270 (2017).

[7] T. R. Kakuda, C. G. Levi, and T. D. Bennett, "The thermal behavior of CMAS-infiltrated thermal barrier coatings," Surface and Coatings Technology **272**, 350–356 (2015).

[8] J. Wu, H. bo Guo, Y. zhi Gao, and S. kai Gong, "Microstructure and thermo-physical properties of yttria stabilized zirconia coatings with CMAS deposits," Journal of the European Ceramic Society **31**, 1881–1888 (2011).

[9] S. Krämer, S. Faulhaber, M. Chambers, D. Clarke, C. Levi, J. Hutchinson, and A. Evans, "Mechanisms of cracking and delamination within thick thermal barrier systems in aero-engines subject to calcium-magnesium-alumino-silicate (CMAS) penetration," Materials Science and Engineering: A **490**, 26–35 (2008).

[10] C. Mercer, S. Faulhaber, A. Evans, and R. Darolia, "A delamination mechanism for thermal barrier coatings subject to calcium–magnesium–alumino-silicate (CMAS) infiltration," Acta Materialia **53**, 1029–1039 (2005).

[11] H. Peng, L. Wang, L. Guo, W. Miao, H. Guo, and S. Gong, "Degradation of EB-PVD thermal barrier coatings caused by CMAS deposits," Progress in Natural Science: Materials International **22**, 461–467 (2012).

[12] M. P. Boyce, "2 - Advanced industrial gas turbines for power generation," in *Combined Cycle Systems for Near-Zero Emission Power Generation*, edited by A. D. Rao (Woodhead Publishing, 2012) pp. 44–102.

[13] G. Costa, B. J. Harder, V. L. Wiesner, D. Zhu, N. Bansal, K. N. Lee, N. S. Jacobson, D. Kapush, S. V. Ushakov, and A. Navrotsky, "Thermodynamics of reaction between gas-turbine ceramic coatings and ingested CMAS corrodents," Journal of the American Ceramic Society **102**, 2948–2964 (2019).

[14] R. Naraparaju, U. Schulz, P. Mechnich, P. Döbber, and F. Seidel, "Degradation study of 7wt.% yttria stabilised zirconia (7YSZ) thermal barrier coatings on aero-engine combustion chamber parts due to infiltration by different CaO–MgO–Al2O3–SiO2 variants," Surface and Coatings Technology **260**, 73–81 (2014).

[15] R. Wellman, G. Whitman, and J. R. Nicholls, "CMAS corrosion of EB PVD TBCs: Identifying the minimum level to initiate damage," International Journal of Refractory Metals and Hard Materials **28**, 124–132 (2010).

[16] S. Krämer, J. Yang, C. G. Levi, and C. A. Johnson, "Thermochemical Interaction of Thermal Barrier Coatings with Molten CaO–MgO–Al2O3–SiO2 (CMAS) Deposits," Journal of the American Ceramic Society **89**, 3167–3175 (2006).

[17] J. Xia, L. Yang, R. T. Wu, Y. C. Zhou, L. Zhang, K. L. Huo, and M. Gan, "Degradation Mechanisms Of Air Plasma Sprayed Free-Standing Yttria-Stabilized Zirconia Thermal Barrier Coatings Exposed To Volcanic Ash," Applied Surface Science **481**, 860–871 (2019).

[18] M. R. Kabir, A. K. Sirigiri, R. Naraparaju, and U. Schulz, "Flow Kinetics of Molten Silicates through Thermal Barrier Coating: A Numerical Study," Coatings **9** (2019), 10.3390/coatings9050332.

[19] B. A. Cavainolo, M. P. Kinzel, R. Naraparaju, and M. R. Kabir, "Simulating CMAS Infiltration of an EB-PVD Thermal Barrier Coating Using the Volume-of-Fluid Method," (2023).

[20] Y. Zhao, H. Zhang, G. Wang, Y. Yang, and W. Tian, "Analysis of Slope Stability Based on Layered Infiltration Theory under Wet-dry Cycle Conditions," KSCE Journal of Civil Engineering , 100028 (2024).

[21] P. Carman, "Fluid flow through granular beds," Chemical Engineering Research and Design **75**, S32–S48 (1997).

[22] R. P. Chapuis and M. Aubertin, "On the use of the Kozeny-Carman equation to predict the hydraulic conductivity of soils," Canadian Geotechnical Journal **40**, 616 – 628 (2003), cited by: 402.

[23] R. Naraparaju, J. J. Gomez Chavez, P. Niemeyer, K.-U. Hess, W. Song, D. B. Dingwell, S. Lokachari, C. V. Ramana, and U. Schulz, "Estimation of CMAS infiltration depth in EB-PVD TBCs: A new constraint model supported with experimental approach," Journal of the European Ceramic Society **39**, 2936–2945 (2019).

[24] D. Benavente, P. Lock, M. A. García Del Cura, *et al.*, "Predicting the Capillary Imbibition of Porous Rocks from Microstructure," Transport in Porous Media **49**, 59–76 (2002).

[25] J. Cai, T. Jin, J. Kou, S. Zou, J. Xiao, and Q. Meng, "Lucas–Washburn Equation-Based Modeling of Capillary-Driven Flow in Porous Systems," Langmuir **37**, 1623–1636 (2021), pMID: 33512167, https://doi.org/10.1021/acs.langmuir.0c03134.

[26] B. Cavainolo and M. Kinzel, "Investigation of Volume-of-Fluid Method to Simulate Melting-Solidification of CMAS Particles," in *ASME 2022 Fluids Engineering Division Summer Meeting*, Vol. Volume 2: Multiphase Flow (MFTC); Computational Fluid Dynamics (CFDTC); Micro and Nano Fluid Dynamics (MNFDTC) (V002T04A002, 2022).

[27] Siemens, "STAR-CCM+ User's Manual," (2023).

[28] J. Zhang, "Lattice Boltzmann method for microfluidics: models and applications," Microfluid Nanofluid **10**, 1–28 (2011).

[29] *A Study of Microfluidic Device Geometries on Fluid Instabilities*, Fluids Engineering Division Summer Meeting, Vol. Volume 2: Multiphase Flow (MFTC); Computational Fluid Dynamics (CFDTC); Micro and Nano Fluid Dynamics (MNFDTC) (2022) https://asmedigitalcollection.asme.org/FEDSM/proceedings-pdf/FEDSM2022/85840/V002T04A013/6923145/v002t04a013-fedsm2022-87470.pdf.

[30] D. Mikaelian and B. Jones, "Modeling of capillary-driven microfluidic networks using electric circuit analogy," SN Applied Sciences **2**, 415 (2020).

[31] P. R. Waghmare and S. K. Mitra, "Finite reservoir effect on capillary flow of microbead suspension in rectangular microchannels," Journal of Colloid and Interface Science **351**, 561–569 (2010).

[32] E. W. Washburn, "The Dynamics of Capillary Flow," Phys. Rev. **17**, 273–283 (1921).

[33] J. Han, Y. Zou, D. Wu, and Y. Zhang, "Investigating the thermal, mechanical and thermal cyclic properties of plasma-sprayed Al2O3-7YSZ/7YSZ double ceramic layer TBCs," Journal of the European Ceramic Society **43**, 4124–4135 (2023).

[34] S. Webb, "Silicate melts: Relaxation, rheology, and the glass transition," Reviews of Geophysics **35**, 191–218 (1997), https://agupubs.onlinelibrary.wiley.com/doi/pdf/10.1029/96RG03263.

[35] A. Bakal, K. Roebbecke, H. Wang, W. Deng, X. Zhang, and J. W. Fergus, "Evolution of the Thermal Conductivity of Sm2Zr2O7 Under CMAS Attack," in *Energy Materials 2017*, edited by X. Liu, Z. Liu, K. Brinkman, S. Das, S. Dryepondt, J. W. Fergus, Z. Guo, M. Han, J. A. Hawk, T. Horita, P. Hosemann, J. Li, E. Olivetti, A. Pandey, R. B. Rebak, I. Roy, C. Shang, and J. Zhang (Springer International Publishing, Cham, 2017) pp. 227–235.

[36] N. P. Bansal and S. R. Choi, "Properties of CMAS glass from desert sand,"

Ceramics International **41**, 3901–3909 (2015).

[37]T. R. Kakuda, A. M. Limarga, T. D. Bennett, and D. R. Clarke, "Evolution of thermal properties of EB-PVD 7YSZ thermal barrier coatings with thermal cycling," Acta Materialia **57**, 2583–2591 (2009).

[38]L. G. Bravo, N. Jain, P. Khare, M. Murugan, A. Ghoshal, and A. Flatau, "Physical aspects of CMAS particle dynamics and deposition in turboshaft engines," Journal of Materials Research **35**, 2249–2259 (2020).

[39]D. Gründing, M. Smuda, T. Antritter, M. Fricke, D. Rettenmaier, F. Kummer, P. Stephan, H. Marschall, and D. Bothe, "A comparative study of transient capillary rise using direct numerical simulations," Applied Mathematical Modelling **86**, 142–165 (2020).

[40]Y. Shiri and S. M. J. Seyed Sabour, "Analytical, experimental, and numerical study of capillary rise dynamics from inertial to viscous flow," Physics of Fluids **34**, 102105 (2022), https://pubs.aip.org/aip/pof/article-pdf/doi/10.1063/5.0111688/16570986/102105_1_online.pdf.

[41]A. Hamraoui and T. Nylander, "Analytical Approach for the Lucas–Washburn Equation," Journal of Colloid and Interface Science **250**, 415–421 (2002).

[42]L. Eça and M. Hoekstra, "A procedure for the estimation of the numerical uncertainty of CFD calculations based on grid refinement studies," Journal of Computational Physics **262**, 104–130 (2014).

[43]I. B. Celik, U. Ghia, P. J. Roache, and C. J. Freitas, "Procedure for estimation and reporting of uncertainty due to discretization in CFD applications," Journal of fluids Engineering-Transactions of the ASME **130** (2008).

[44]K. Chandran, S. Rittgers, and A. Yoganathan, *Biofluid Mechanics: The Human Circulation, Second Edition*, 2nd ed. (CRC Press, 2012).

[45]H. Zhao, C. G. Levi, and H. N. Wadley, "Molten silicate interactions with thermal barrier coatings," Surface and Coatings Technology **251**, 74–86 (2014).